machines

Article

Optimized Hydrodynamic Design for Autonomous Underwater Vehicles

Gang Fan [1,*], Xiaojin Liu [1], Yanan Hao [1], Guoling Yin [1] and Long He [2,*]

[1] Department of Electrical Engineering, Taiyuan Institute of Technology, Taiyuan 030008, China; liuxiaojin@tit.edu.cn (X.L.); haoyn@tit.edu.cn (Y.H.); yinguoling@tit.edu.cn (G.Y.)
[2] School of Mechanical and Electrical Engineering, North University of China, Taiyuan 030051, China
* Correspondence: fangang@tit.edu.cn (G.F.); b20230107@st.nuc.edu.cn (L.H.)

Abstract: In this study, the drag coefficient and lift-to-drag ratio variation with angle of attack and velocity are analyzed by numerical simulation of the hydrodynamics of the initial shape of an autonomous underwater vehicle (AUV). Based on this, the response surface method (RSM) and multi-objective genetic algorithm (MOGA) are used to optimize the geometric parameters of the shape, aiming to improve the lift-to-drag ratio and reduce the mass. In the study, a second-order response surface model was constructed to analyze the relationship between the target variables and the structural geometric parameters, and the MOGA algorithm effectively searched for the globally optimal solution. The optimization results show that the lift-to-drag ratio is increased from 0.684 to 0.778 and the mass of the shell is reduced from 26.6 kg to 24.06 kg, which significantly improves the hydrodynamic performance of the AUV. The optimization method not only improves the performance of the AUV, but also provides a valuable reference for its hydrodynamic design, which has a good application prospect.

Keywords: AUV; shape optimization; multi-objective optimization; response surface method

1. Introduction

Autonomous underwater vehicles (AUVs) are important tools for ocean exploration, playing a key role in resource development and environmental monitoring. Their efficient and stable operation is inseparable from good hydrodynamic shape design [1]. By optimizing the shape of AUVs, not only can their anti-interference ability be enhanced and energy consumption reduced, but they can also better adapt to the needs of diversified tasks. Many scholars have conducted in-depth research on the motion performance of AUVs. For example, in [2], aiming at the problem of large wave resistance of traditional torpedo-shaped AUVs operating near the free surface, the first-order Rankine panel method and simulated annealing algorithm were used to optimize the hull shape, successfully reducing the wave resistance and verifying the optimization effect through experiments. Sun et al. studied the body shape of humpback whales and used the response surface method to optimize the bionic hull shape from the perspectives of drag and volume, improving the spatial utilization rate and range of AUVs [3]. The optimization effect was verified in both simulations and towing tests. Gao et al. proposed an AUV hull shape optimization platform based on the multi-island genetic algorithm (MIGA), using unstructured 2D grids and adaptive strategies to improve computational efficiency and accuracy [4]. In the field of underwater gliders, Wang et al. designed a new type of underwater glider based on the BWB configuration. Through high-precision numerical analysis and surrogate models, and by applying particle swarm optimization algorithms for hydrodynamic optimization, the

check for updates

Academic Editor: Yahui Liu

Received: 21 January 2025
Revised: 24 February 2025
Accepted: 27 February 2025
Published: 28 February 2025

Citation: Fan, G.; Liu, X.; Hao, Y.; Yin, G.; He, L. Optimized Hydrodynamic Design for Autonomous Underwater Vehicles. *Machines* **2025**, *13*, 194. https://doi.org/10.3390/machines13030194

hydrodynamic performance was improved by 9.1% [5]. Yang et al., based on approximate model techniques, optimized the shape of the underwater glider with the goal of minimizing the drag coefficient. They considered the size coupling relationship and analyzed the effects of load and pitch angle on the shape. The effectiveness of the CFD simulation method was verified through circulating water channel experiments [6]. Li et al. aimed to maximize the lift-to-drag ratio of the glider and established a Kriging surrogate model, using the EGO algorithm to optimize the shape of the tandem-wing glider [7]. Zhang et al. proposed a shape optimization framework based on NURBS parameterization and Kriging models, aiming to maximize the lift-to-drag ratio and improve optimization efficiency [8,9]. By using the NURBS method to achieve flexible shape deformation, a Kriging optimization framework with dynamic filling of sample points was established, further improving the optimization efficiency. Wang et al. [10] used Kriging as a surrogate model and, based on the free deformation parameter method and a sequential Bayesian optimization algorithm, optimized the hydrofoils of an underwater glider, thereby enhancing its hydrodynamic performance.

In other fields, the effect of vortex generators (VGs) on the hydrodynamic performance of a submarine at a high angle of attack has been studied using multi-objective optimization and computational fluid dynamics (CFD) [11]. The results showed that the optimal geometry of VGs could significantly improve the submarine's hydrodynamic performance by reducing drag and lift coefficients. Similarly, the optimization of roof-flap geometry and position for simultaneous drag and lift reduction has been explored using CFD-based multi-objective optimization [12]. The study demonstrated that the optimized roof-flap design could effectively reduce the drag and lift coefficients of a vehicle. In the field of automotive aerodynamics, the impact of canard design on wake control behind a car has been investigated using artificial neural networks (ANN) and genetic algorithms (GA) [13]. The research indicated that the optimized canard design could reduce the drag and lift coefficients, thereby improving the car's fuel efficiency. Additionally, advanced computational techniques such as ANN and evolutionary algorithms have been utilized to predict the viscosity and thermal conductivity of nanofluids [14]. These studies highlight the potential of multi-objective optimization and CFD in enhancing the hydrodynamic performance of various vehicles, which can be leveraged to improve the design of AUVs.

Despite advancements in AUV optimization, a gap remains in the comprehensive application of multi-objective optimization techniques, particularly in balancing the trade-offs between lift-to-drag ratio and mass reduction. To address this, this study conducts a hydrodynamic numerical simulation of an AUV's initial shape, analyzing the variation of drag coefficient and lift-to-drag ratio with respect to the angle of attack and velocity. Based on this analysis, the response surface method (RSM) and a multi-objective genetic algorithm (MOGA) are applied to optimize the geometric parameters of the AUV's shape. A second-order response surface model is constructed to examine the relationship between the target variables and the geometric parameters, while the MOGA algorithm efficiently searches for the global optimal solution. This approach enhances the AUV's hydrodynamic performance by improving the lift-to-drag ratio and reducing its mass.

The remainder of this paper is organized as follows: Section 2 presents the hydrodynamic parameter calculations, including the validation of numerical methods and the numerical calculations and analysis of results. Section 3 details the optimization analysis, covering the optimization of design methods and the multi-objective genetic algorithm and result analysis. Finally, Section 4 concludes the study and provides an outlook for future research.

2. Hydrodynamic Parameter Calculations

A detailed model of the AUV was constructed on the basis of the laboratory program. The model comprehensively considers the key structural parameters of the AUV, as shown in Table 1. During the mission, AUV inevitably encounters challenges from multiple environmental factors, such as waves and currents, and its hydrodynamic performance becomes a key indicator of the success or failure of AUV design, as well as the root of realizing precise control and fine operation. In the design process, the bow curve AB of AUV adopts a two-parameter elliptic curve, while the stern curve CD adopts a conical curve design, with overall simple lines and low processing cost, as shown in Figure 1, in which the radius of gyration Q is 84 mm and the total length L_T is divided into four parts: the length of bow section L_1, the length of stern section L_2, the length of middle section L, and the length of the stern propeller protrusion. To facilitate the convergence of the calculation results and enhance the computational speed, the AUV model was simplified before meshing. Specifically, parts that have less influence on the hydrodynamic performance but are prone to complex meshing were omitted, without changing the overall shape and structure of the AUV. The simplified features mainly include small chamfers and bolt heads, which are known to create meshing difficulties and significantly increase computational complexity. These features have minimal impact on the overall flow field and hydrodynamic performance of the AUV. A right-handed inertial coordinate system is adopted, with the center of buoyancy of the AUV at static as the coordinate origin, where the x-axis positive direction is along the origin to the bow, the y-axis positive direction is along the origin to the left, and the z-axis positive direction is perpendicular to the fuselage upward. As shown in Figure 2, the hydrodynamic model and coordinate system of the AUV are presented.

Table 1. Structural parameters.

Parameters	Symbol	Value
total mass of the vehicle	m	35.52 kg
total length	L_T	1725 mm
maximum diameter	D_m	178 mm
drainage volume	V	34.5 dm^3
length of bow section	L_1	165 mm
length of stern section	L_2	245 mm
length of middle section	L	1235 mm
maximum speed	v	3.5 m/s

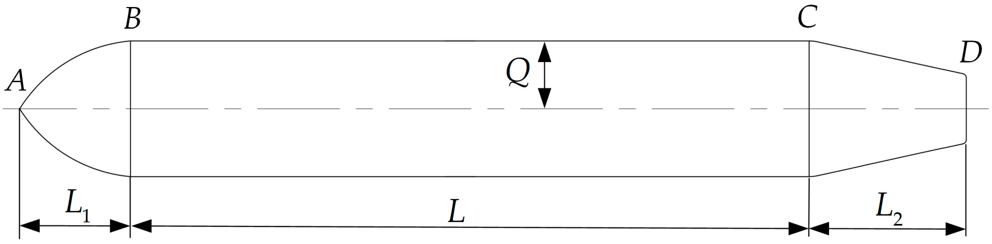

Figure 1. AUV linetype.

2.1. Validation of Numerical Methods

In order to ensure the reliability of the numerical calculation results, the validity of the calculation method used in this paper is verified using the “SEAGULL” underwater glider developed by Shanghai Jiao Tong University. The “SEAGULL” glider, designed for a maximum depth of 500 m, features a total length of 2.04 m and a weight of 68.00 kg in air. It comprises a buoyancy adjustment mechanism, attitude adjustment mechanism, control system, communication and positioning system, and a general structure. The “SEAGULL” glider has been validated through lake trials, demonstrating stable performance and maneuverability [15]. The “SEAGULL” glider and its mesh division are shown in Figure 3. The drag values of the model were calculated at an angle of attack of 0° and velocities of 0.2 m/s, 0.3 m/s, 0.4 m/s, and 0.5 m/s, respectively. These values were compared with the results of the pool towing test. The comparison curves are shown in Figure 4, demonstrating that the differences between the two sets of values are relatively small, thereby validating the numerical computation method used.

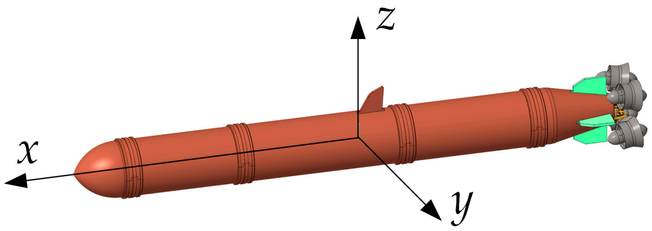

Figure 2. Hydrodynamic model and its coordinate system.

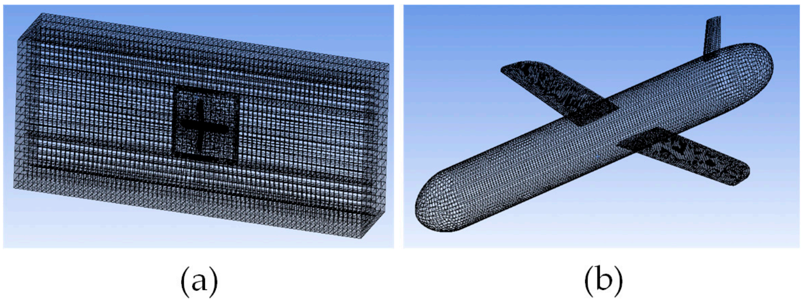
(a)
(b)

Figure 3. Schematic diagram of model meshing: (**a**) overall meshing diagram, (**b**) detailed meshing of the model.

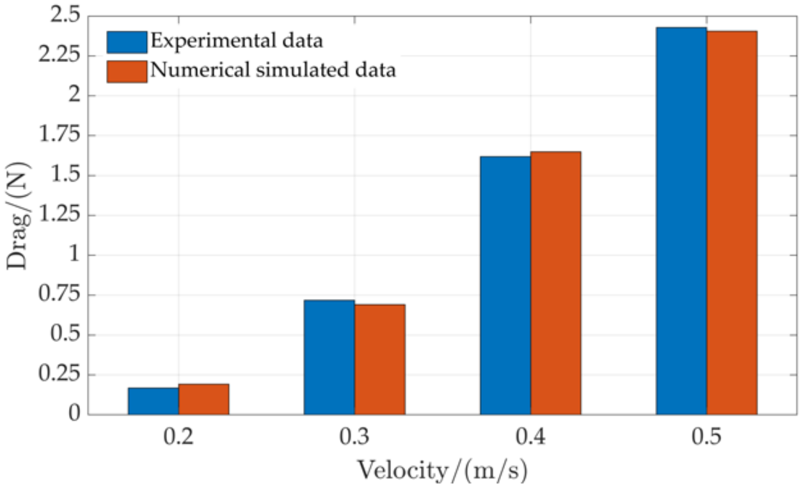

Figure 4. Comparison of numerical simulation results and experimental results.

2.2. Numerical Calculations and Analysis of Results

The speed requirement of our designed micro vehicle does not exceed 4 m/s, which falls into the category of low-speed navigation. At this speed, the viscous drag of water has a particularly significant effect on AUVs, and the proportion of viscous drag in the total drag increases as the speed decreases. Therefore, the key to the hydrodynamic performance of AUVs lies in the calculation and analysis of water resistance.

The CFD solver used in this study is ANSYS Fluent 2021, employing the finite volume method (FVM) for numerical discretization. A second-order upwind scheme is applied to the convective and diffusive terms to reduce numerical diffusion and improve accuracy in boundary-layer and flow-separation predictions. Pressure-velocity coupling is handled using the SIMPLEC algorithm, while a least-squares cell-based method is used for gradient reconstruction. The residual convergence criterion is set to 10^{-4}, ensuring iterative errors for all governing equations are reduced to below 0.01% of their initial values.

To accurately simulate turbulent flow at low Reynolds numbers, this study employs the Reynolds-Averaged Navier–Stokes (RANS) method with the k-ω SST turbulence model, avoiding the need for complex damping functions required in the k-ε model.

The computational domain is divided into two regions:

1. Global Computational Domain: simulating the ocean environment using a $16\,L \times 10\,L \times 10\,L$ cuboid region;
2. Local Computational Domain: modeling the AUV's position as a $5\,L$ diameter sphere, with the center of buoyancy set as the sphere's center.

For the complex and irregular geometry of the AUV, an unstructured tetrahedral mesh is applied. To enhance the accuracy of drag coefficient predictions, the boundary layer near the AUV surface is locally refined. Prism-layer meshing is used, with 10 layers of prism elements expanding in a geometric progression. The first-layer mesh height is set to 0.05 mm, ensuring a y^+ value of approximately 6 for accurate resolution of the viscous sublayer. The computational mesh consists of approximately 1.1 million unstructured tetrahedral elements, ensuring sufficient resolution for accurate flow predictions while maintaining computational efficiency. The average cell quality is 0.85, which is considered good for CFD simulations, as values above 0.8 typically indicate a well-structured mesh with minimal numerical errors. This quality metric, ranging from 0 to 1, is based on factors such as aspect ratio, skewness, and orthogonality, where 1 represents an ideal equilateral element.

Boundary conditions:

1. Inlet: defined as a uniform velocity inlet, simulating seawater at 15 °C (density 1026 $\mathrm{kg/m^3}$, dynamic viscosity 0.0009 Pa·s);
2. Outlet: set as a pressure outlet with a pressure of 0 Pa;
3. AUV Surface: treated as a no-slip wall;
4. Computational Domain Boundaries (Far-field): assigned specified pressure gradient boundary conditions.

The angle of attack α ranges from -20° to 20° in the numerical calculation; the velocity v ranges from 0.5 m/s to 4 m/s. The lift-to-drag ratio Z is defined as the ratio of the lift coefficient C_l to the drag coefficient C_d. The drag coefficient C_d with α and the lift-to-drag ratio Z with α are obtained by 100 sets of simulations and summarizing the data, as shown in Figures 5 and 6.

From Figure 5, it can be seen that the drag coefficient C_d increases with the increase of α and v. When $\alpha = 0^\circ$, the head-on area of the AUV is the smallest, so the drag force is the smallest at this time; the head-on area increases correspondingly with the increase of α, and the drag force of the AUV increases as well. Since the AUV is not a completely symmetrical structure, the trend of the drag coefficient C_d is not completely symmetrical at $\alpha < 0^\circ$ and $\alpha > 0^\circ$.

Figure 6 shows that the lift-to-drag ratio increases with the angle of attack, but the peak value does not exceed 0.9, implying that the AUV consumes more energy in sustaining the motion, so the shape optimization is particularly important. The growth of the lift-to-drag ratio curve slows down when the angle of attack is less than -15° or more than 15°.

Combined with the drag coefficient change in Figure 5, we select $v = 4$ m/s and $\alpha = 15°$ as the key point for optimization; at this time, $C_d = 0.282$ and $C_l = 0.193$.

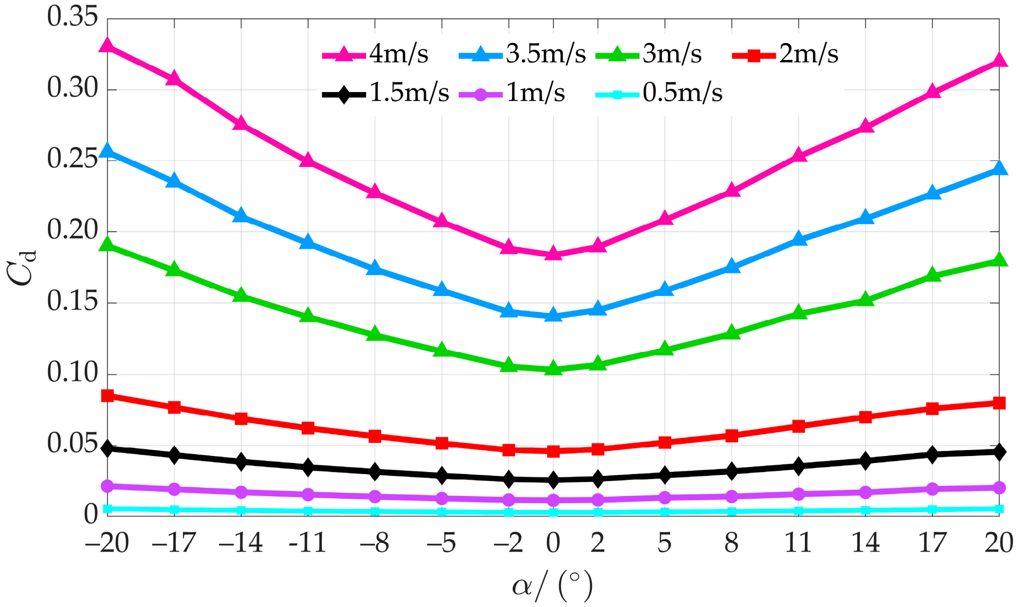

Figure 5. Variation curve of drag coefficient with angle of attack.

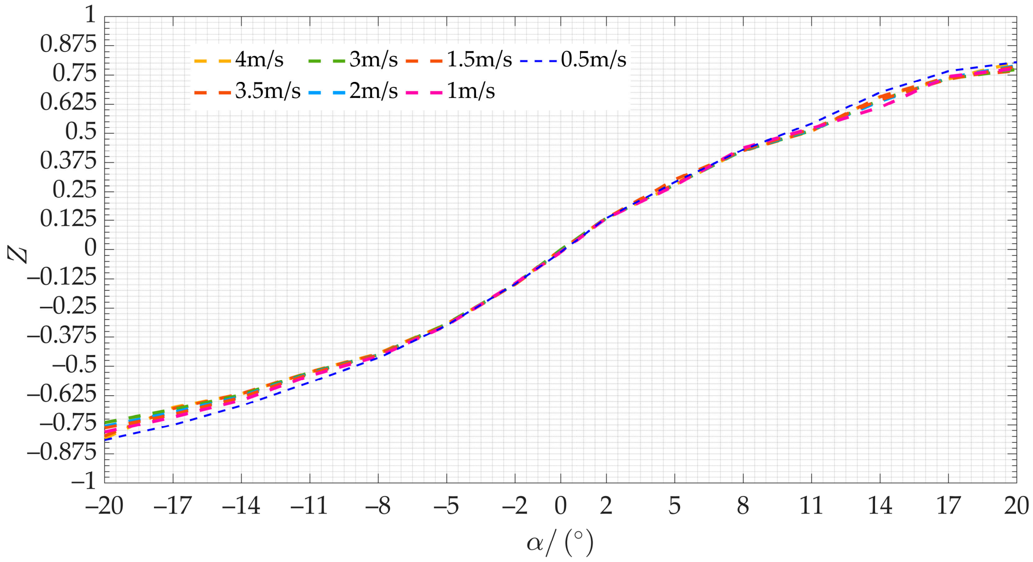

Figure 6. Lift-to-drag ratio curve.

3. Optimization Analysis

Considering the substantial workload and the extensive time required for optimization calculations when directly employing Computational Fluid Dynamics (CFD) methods, we opted to develop a response surface model. This model establishes a relationship between the AUV's profile structural parameters and its hydrodynamic characteristics [16]. By leveraging the objective function and the optimization algorithm, our goal is to achieve the most optimal hydrodynamic shape. The optimization process is elaborately depicted in Figure 7. The core objective of the optimization design is to adjust the shell geometry to enhance the lift-to-drag ratio, improve the hydrodynamic performance, and reduce the weight of the AUV. The mathematical formulation of this multi-objective optimization problem is as follows:

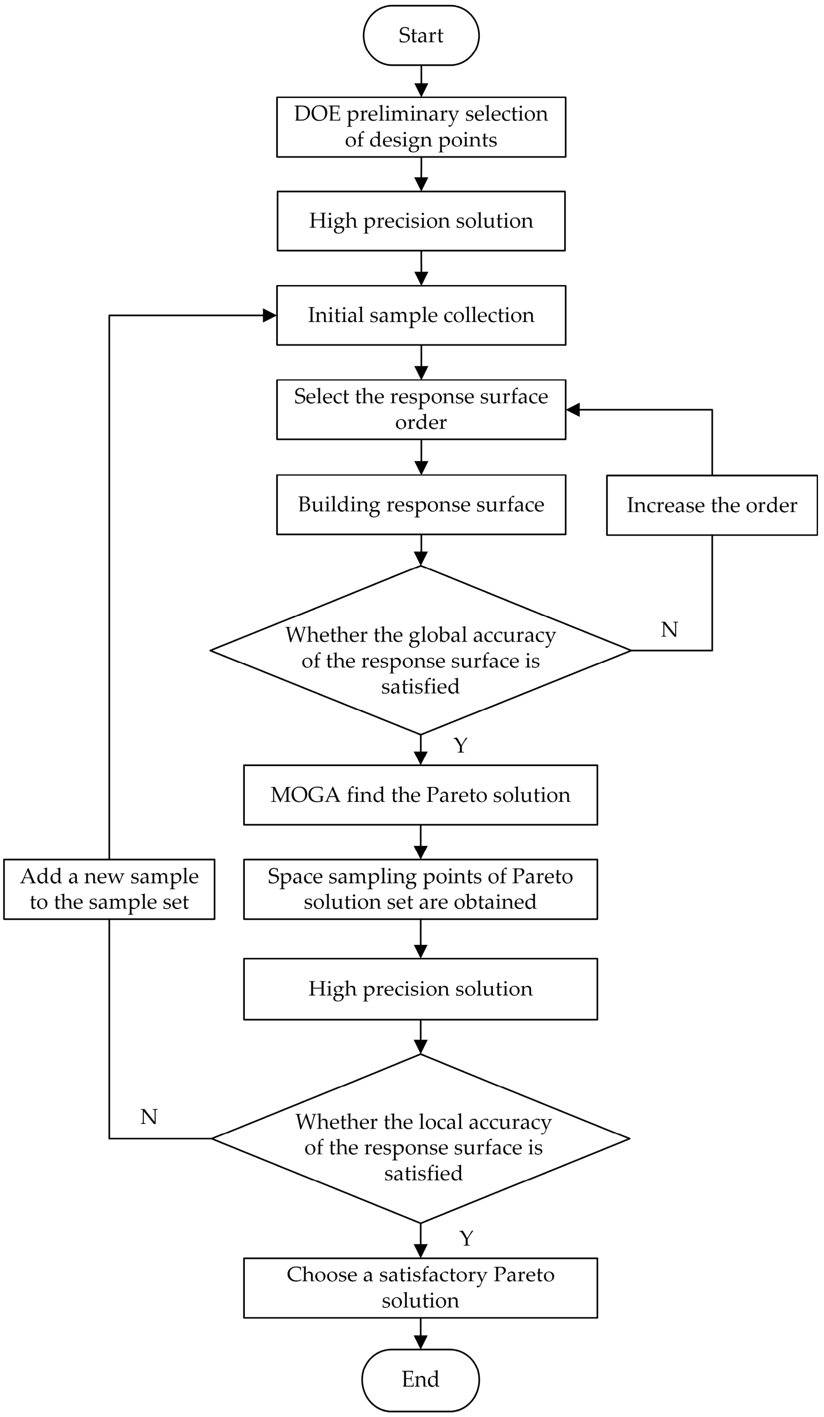

Figure 7. Optimization flow chart.

Objective function: $\max Z_x(x)$, $\min W_x(x)$, Constraints: $a_i \leq x_i \leq b_i$.

Where the design variables $x = [x_1, x_2, x_3, x_4]$ are the main geometrical parameters $[L_1, L_2, Q, L]$ of the shell, the objective function Z_x and W_x are the lift-to-drag ratio and the structural mass, respectively. In the study, a_i and b_i represent the upper and lower limits of the values of each geometric parameter, respectively. These limits were set to 10% of the initial parameter values, which provided a reasonable range for optimization without violating the design constraints.

3.1. Optimization of Design Methods

Response surface analysis is a statistical method for solving multivariate problems. In order to clarify the relationship between the design variables and the response values, the Latin Hypercubic Sampling (LHS) method is used to lay out the test sample points using the principle of random orthogonal distribution with equal probability [17,18], so as to obtain a more accurate response surface model by using fewer sample points.

Response surface fitting is used to fit the relationship between the design variables and the response values by establishing certain functional relationships based on the test sample points. A second-order polynomial is chosen for fitting and the mathematical expression is

$$\hat{y}(x) = \beta_0 + \sum_{i=1}^{n} \beta_i x_i + \sum_{i=1}^{n} \beta_{ii} x_i^2 + \sum_{i=1}^{n-1} \sum_{j=i+1}^{n} \beta_{ij} x_i x_j \tag{1}$$

where $\hat{y}(x)$ is the predicted value of the response surface, x_i is the ith component of the independent variable, and β_0, β_i, β_{ii}, and β_{ij} are the regression coefficients. To evaluate the predictive capability of the response surface, we employ the R^2 and the root mean square error σ to assess the fitting accuracy of the response surface [19]. The calculation formulas are as follows:

$$R^2 = 1 - \frac{\sum\limits_{i=1}^{n} (y_i - \hat{y}_i)^2}{\sum\limits_{i=1}^{n} y_i{}^2 - \sum\limits_{i=1}^{n} \hat{y}_i^2 / n} \tag{2}$$

$$\sigma = \sqrt{\frac{\sum\limits_{i=1}^{n} (y_i - \hat{y}_i)^2}{n}} \Bigg/ \frac{\sum\limits_{i=1}^{n} y_i}{n} \tag{3}$$

where y_i denotes the observed values at the design points. When R^2 is close to 1 and σ is close to 0, the fitting precision of the response surface is higher.

The specific evaluation results are shown in Table 2, where R^2 of all target variables exceed 0.96 and σ are well below 0.1, satisfying the accuracy requirements. The relative importance of the design variables L_1, L_2, Q, and L on the lift coefficient C_l, drag coefficient C_d, mass W, and lift-to-drag ratio Z are given by the localized sensitivity diagram in Figure 8. L_1, L_2, Q, and L have a significant influence on C_l and C_d. Among them, the middle section length L has the most significant effect on these parameters; the bow section length L_1 has a greater effect on the lift and drag coefficients than the stern section length L_2, and the effect of L_2 is opposite to that of L_1. The effect of shell turning radius Q on lift and drag coefficients is greater than that of L_2, and its effect is also opposite to that of L_2. For the lift-to-drag ratio, the effect of Q is greater than that of L_1, which in turn is greater than that of L_2. In the case of mass W, the effect of L_1 is greater than that of L_2, and the effect of L_2 is greater than that of Q.

Table 2. Fitting accuracy evaluation results.

Target Variables	R^2	σ
Z	0.967	0.053
W	0.992	0.005

Figures 9 and 10 show the trends of lift-to-drag ratio Z and mass W with L_1, L_2, Q, and L. Figure 9 shows that the lift-to-drag ratio increases with increasing L_1 and decreases with increasing L_2. In order to maximize Z, L_1 and L_2 should be close to the endpoints of their range of values. The lift-to-drag ratio is very sensitive to changes in the length of L and Q, and Z is maximized at the right endpoint of the range of values, where L has the most significant effect on Z. Figure 10 shows that mass W is linearly related to these variables and is particularly affected by L. All variables should be taken close to the left end of their range.

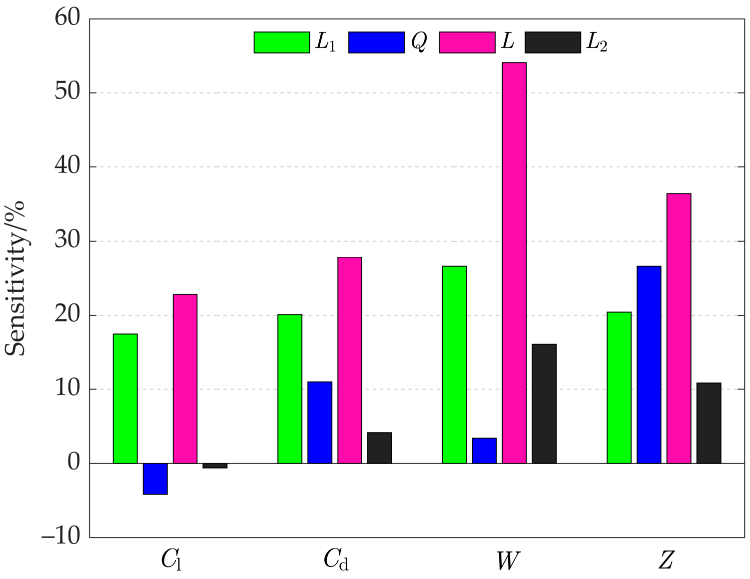

Figure 8. Sensitivity diagram.

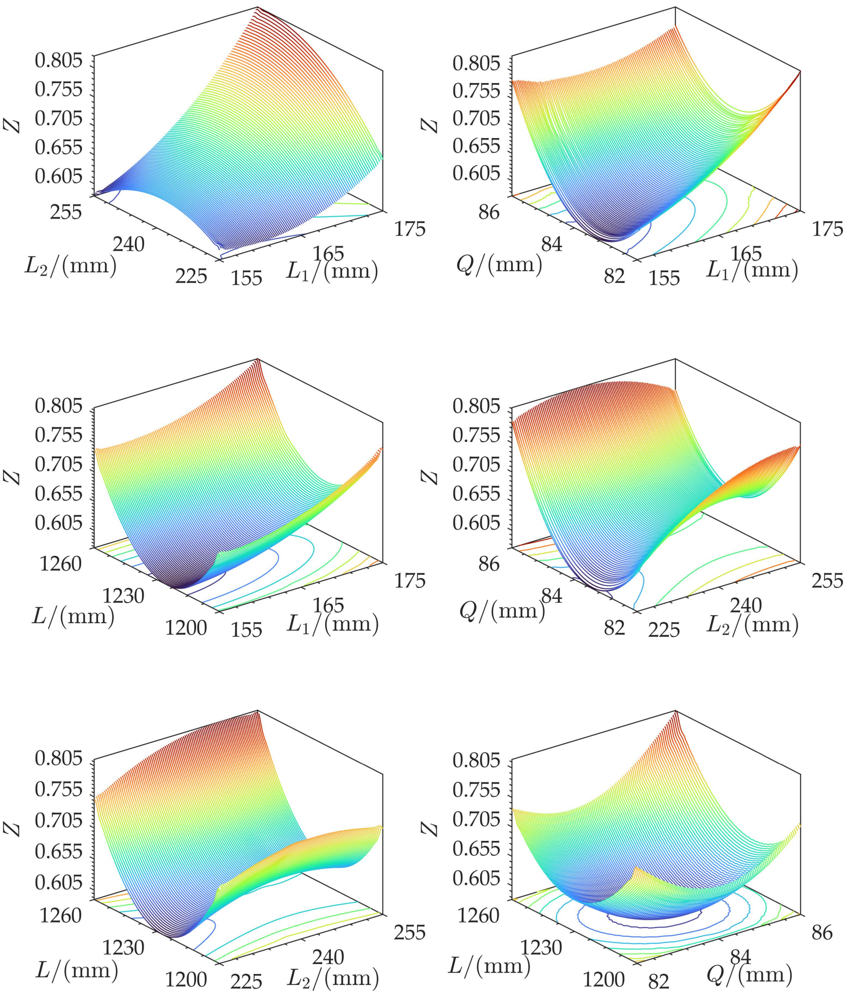

Figure 9. Response surface when output is Z.

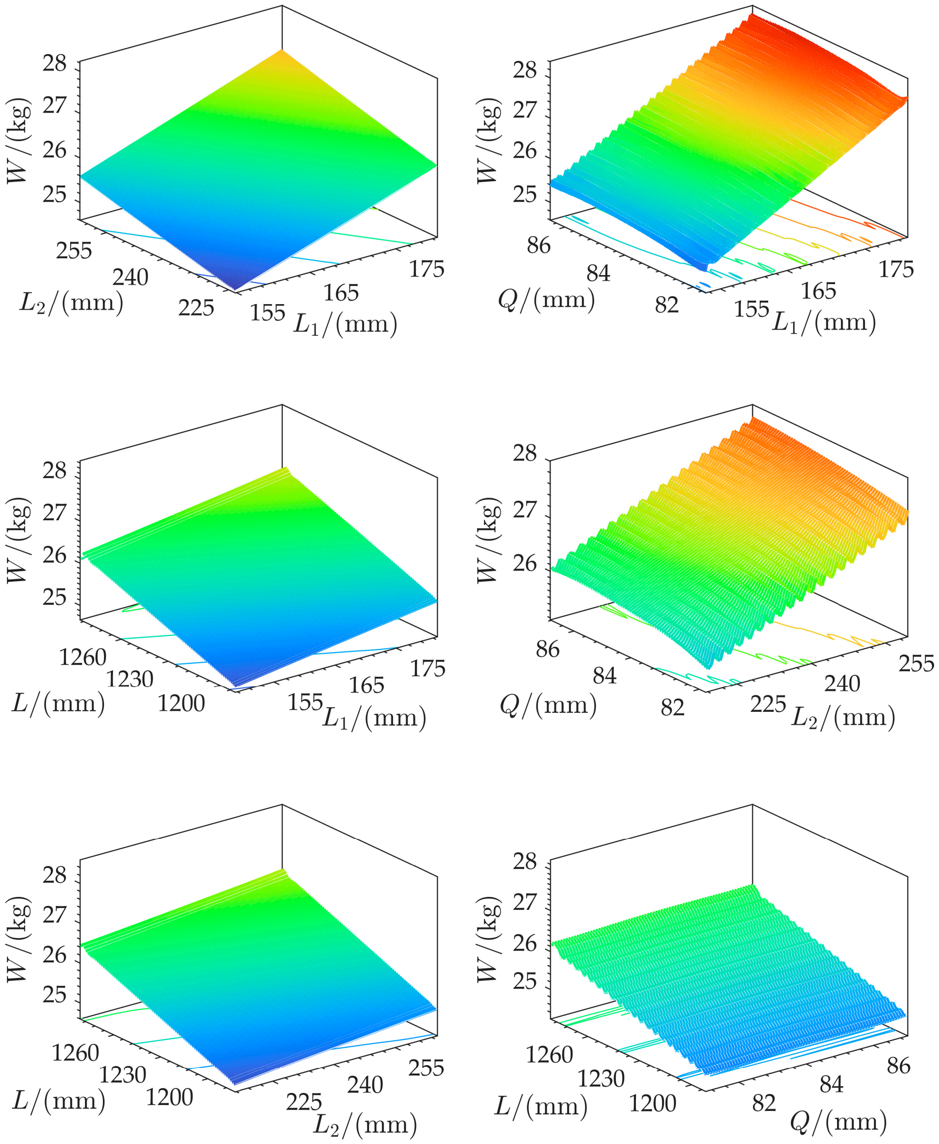

Figure 10. Response surface when output is *W*.

Through the above analysis, it can be seen that there is a mutually exclusive relationship between the four design variables, and taking into account the actual processing and manufacturing and internal assembly of some spatial constraints, *Z* and *W* cannot reach the optimal value at the same time, so it is necessary to carry out algorithmic optimization to constitute all possible solutions into the optimal solution set of Pareto [20], which is a set of solutions that improves a certain objective variable at the expense of the other objective variables.

3.2. Multi-Objective Genetic Algorithm and Result Analysis

In order to find the optimal equilibrium point between the target variables, 400 sample points are selected by using the offset Hammersley sampling (SHS) technique, and the optimization design problem is optimized by a multi-objective genetic algorithm. The multi-objective genetic algorithm was selected for this study due to its efficiency in handling multi-objective optimization problems and its ability to provide a well-distributed set of Pareto optimal solutions. Compared to NSGA-II, MOGA offers a simpler and more efficient approach, providing a good balance between exploration and exploitation while maintaining a diverse set of solutions. This makes MOGA particularly suitable for optimizing the AUV's geometric parameters to achieve the desired trade-offs between the lift-to-drag ratio and mass reduction. The other parameter settings of the MOGA algorithm are shown in Table 3. Calculate whether Z and W satisfy the termination condition. If they do, the termination population is generated; if they do not, the next generation population is obtained through the process of fitness assignment and so on. Continue to judge until the termination condition is satisfied [21]. The convergence behavior of the algorithm is illustrated in Figure 11, which shows the evolution of the lift-to-drag ratio Z and mass W over successive iterations. Initially, Z increases rapidly as the genetic algorithm explores the search space, while W decreases significantly. As the number of generations increases, the changes in both parameters gradually stabilize, indicating convergence toward an optimal solution. The convergence graph demonstrates that the optimization process reaches a stable solution after a sufficient number of iterations, ensuring that further increases in generations provide minimal improvements. This validates the efficiency of the optimization framework. The distribution of the Pareto optimal solution set is obtained through several iterations, as shown in Figure 12. The color of the dots represents the quality of the results, with dark blue indicating the optimal solutions and yellow indicating the worst. The red ellipse region marks the optimal boundary. Table 4 shows the three Pareto optimal solutions selected based on merit.

Table 3. MOGA parameters.

Parameters	σ
percentage of convergence stabilization	100%
maximum allowable Pareto percentage	75%
crossover rate	0.9
variation rate	0.1

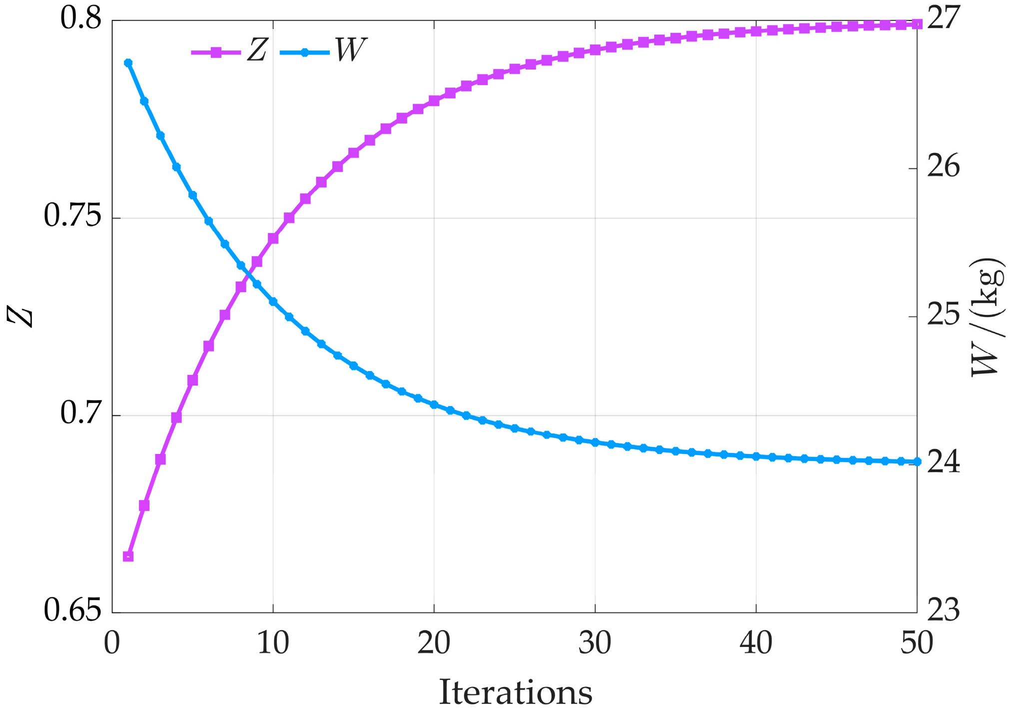

Figure 11. Convergence graph.

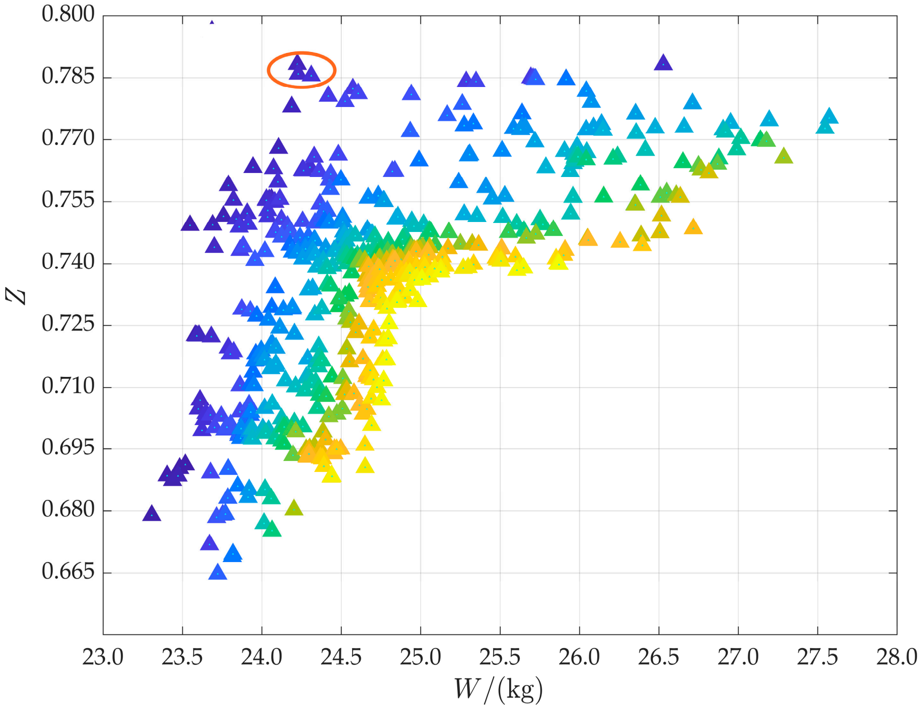

Figure 12. Distribution of Pareto solution sets.

Table 4. Pareto optimal solutions.

Title	***Z***	***W*/kg**	**L_1/mm**	**L_2/mm**	***Q*/mm**	***L*/mm**
optimization point 1	0.788	24.06	174.5	227.4	85.1	1203.4
optimization point 2	0.787	24.11	173.1	227.9	85.6	1208.3
optimization point 3	0.786	24.28	170.9	229.1	86.6	1212.1

Optimization point 1, which exhibits the largest lift-to-drag ratio and a relatively small mass in the calculation, was selected as the final design result. This selection was based on a balanced consideration of both hydrodynamic performance and structural efficiency, with each objective weighted equally at 50%. At this time, the drag coefficient $C_d = 0.274$ and the lift coefficient $C_l = 0.216$; the detailed data comparison before and after the optimization design is shown in Table 5. The optimized lift-to-drag ratio Z and mass W are both better than the initial values, indicating that the hydrodynamic performance of the optimized AUV profile is better than the original profile.

Table 5. Comparison of data before and after optimization.

Title	***Z***	***W*/kg**	**L_1/mm**	**L_2**	***Q*/mm**	***L*/mm**
result before optimization	0.684	26.6	165	245	84	1235
optimized results	0.788	24.06	174.5	227.4	85.1	1203.4

In order to verify the accuracy of the optimization results, numerical calculations were re-performed using the data of the design variables from the optimization points [22]. The validation results for the lift-to-drag ratio are shown in Table 6, and it can be seen that the optimization gives a maximum relative error of 1.399% with respect to the numerical calculations. The observed deviations between the optimization results and the numerical calculations can be attributed to several factors. First, the response surface model used in the optimization process is based on a second-order polynomial fit, which inherently introduces some approximation errors. This model is constructed using previously obtained data points and may not perfectly capture the complex nonlinear relationships in the actual system. Second, numerical approximations in the finite volume method (FVM) and the second-order upwind scheme used for discretization can also contribute to minor discrepancies. Despite these minor deviations, the overall agreement between the optimization results and the numerical calculations demonstrates the reliability of the optimization method. The final shape produced is shown in Figure 13.

Table 6. Verification results of lift-to-drag ratio.

Title	Optimal Value	Calculated Value	Relative Error
optimization point 1	0.788	0.778	1.269%
optimization point 2	0.787	0.776	1.397%
optimization point 3	0.786	0.775	1.399%

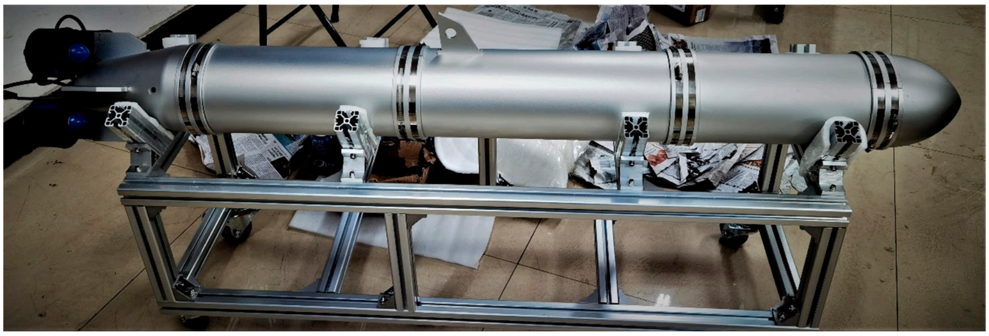

Figure 13. Final shape.

4. Conclusions

Through comprehensive CFD numerical calculations and hydrodynamic performance analysis of the AUV profile, this study investigates the trends of the drag coefficient and lift-to-drag ratio while employing response surface analysis for profile optimization. By integrating orthogonal test design, response surface fitting, sensitivity analysis, and a multi-objective genetic algorithm, the optimization study of the profile parameters was successfully conducted. The results indicate that within the defined parameter range, a larger slewing radius enhances the lift-to-drag ratio but also increases structural mass. Additionally, an increase in AUV length leads to a significant rise in drag coefficient, which negatively impacts both lift-to-drag ratio enhancement and structural mass reduction. Therefore, optimizing the AUV length appropriately is crucial. Under identical radius and length conditions, increasing the bow section length or decreasing the stern section length contributes to an improved lift-to-drag ratio.

While this study primarily focuses on optimizing the lift-to-drag ratio and mass, several critical factors remain unaddressed and warrant further exploration. Future research should consider the following aspects:

1. Dynamic Stability: The current optimization does not incorporate dynamic stability considerations. Future studies should integrate dynamic stability analysis to ensure that the optimized design maintains stable motion across various operating conditions;
2. Performance in Varied Flow Conditions: The AUV's performance under different flow conditions, such as varying flow velocities and directions, should be examined. Numerical simulations and experimental tests can help validate the robustness of the optimized design;
3. Experimental Validation: This study primarily relies on numerical simulations to confirm the optimization results. However, practical experiments are essential for

evaluating the AUV’s real-world performance. Future work should include experimental validation in a towing tank or open-water environment to verify numerical predictions and enhance the design’s reliability.

Author Contributions: Conceptualization, L.H.; resources, G.F.; methodology, X.L.; software, Y.H.; writing—original draft preparation, G.Y. All authors have read and agreed to the published version of the manuscript.

Funding: This research was funded by the Research Grant Program for Introducing Talents to Taiyuan Institute of Technology, grant numbers 2024KJ027 and 2024KJ028. This research was funded by the Research Funding Project for Outstanding Doctors (Post-doctors) Working in Shanxi, grant numbers 2025LJ015.

Data Availability Statement: Data are contained within the article.

Acknowledgments: The authors would like to express their sincere gratitude to the reviewers for their valuable time and professionalism. The reviewers’ critical comments and suggestions for improvement played a key role in enhancing the quality and completeness of this paper, enabling this study to be presented to a wider audience in a more rigorous form.

Conflicts of Interest: The authors declare no conflicts of interest.

References

1. Hong, L.; Wang, X.; Zhang, D.-S. CFD-Based Hydrodynamic Performance Investigation of Autonomous Underwater Vehicles: A Survey. *Ocean Eng.* **2024**, *305*, 117911. [CrossRef]
2. Alvarez, A.; Bertram, V.; Gualdesi, L. Hull Hydrodynamic Optimization of Autonomous Underwater Vehicles Operating at Snorkeling Depth. *Ocean Eng.* **2009**, *36*, 105–112. [CrossRef]
3. Sun, T.; Chen, G.; Yang, S.; Wang, Y.; Wang, Y.; Tan, H.; Zhang, L. Design and Optimization of a Bio-Inspired Hull Shape for AUV by Surrogate Model Technology. *Eng. Appl. Comput. Fluid Mech.* **2021**, *15*, 1057–1074. [CrossRef]
4. Gao, T.; Wang, Y.; Pang, Y.; Cao, J. Hull Shape Optimization for Autonomous Underwater Vehicles Using CFD. *Eng. Appl. Comput. Fluid Mech.* **2016**, *10*, 599–607. [CrossRef]
5. Wang, Z.; Yu, J.; Zhang, A.; Wang, Y.; Zhao, W. Parametric Geometric Model and Hydrodynamic Shape Optimization of a Flying-Wing Structure Underwater Glider. *China Ocean Eng.* **2017**, *31*, 709–715. [CrossRef]
6. Yang, M.; Wang, Y.; Yang, S.; Zhang, L.; Deng, J. Shape Optimization of Underwater Glider Based on Approximate Model Technology. *Appl. Ocean Res.* **2021**, *110*, 102580. [CrossRef]
7. Li, T.; Wang, P.; Sun, B.; Li, C. A Shape Optimization Design Method of the Joined-Wing Underwater Glider. *J. Harbin Inst. Technol.* **2019**, *51*, 26–32.
8. Zhang, D.; Wang, Z.; Ling, H.; Zhu, X. Kriging-Based Shape Optimization Framework for Blended-Wing-Body Underwater Glider with NURBS-Based Parametrization. *Ocean Eng.* **2021**, *219*, 108212. [CrossRef]
9. Zhang, D.; Zhang, B.; Wang, Z.; Ling, H.; Zhang, L. Optimal Design of Hydrodynamic and Shape of Blended-Wing-Body Underwater Glider. *Ship Eng.* **2021**, *43*, 117–123.
10. Wang, X.; Song, B.; Wang, P.; Sun, C. Hydrofoil Optimization of Underwater Glider Using Free-Form Deformation and Surrogate-Based Optimization. *Int. J. Nav. Archit. Ocean Eng.* **2018**, *10*, 730–740. [CrossRef]
11. Rostamzadeh-Renani, M.; Rostamzadeh-Renani, R.; Baghoolizadeh, M.; Khabazian Azarkhavarani, N. The Effect of Vortex Generators on the Hydrodynamic Performance of a Submarine at a High Angle of Attack Using a Multi-Objective Optimization and Computational Fluid Dynamics. *Ocean Eng.* **2023**, *282*, 114932. [CrossRef]
12. Rostamzadeh-Renani, M.; Baghoolizadeh, M.; Sajadi, S.M.; Rostamzadeh-Renani, R.; Azarkhavarani, N.K.; Salahshour, S.; Toghraie, D. A Multi-Objective and CFD Based Optimization of Roof-Flap Geometry and Position for Simultaneous Drag and Lift Reduction. *Prop. Power Res.* **2024**, *13*, 26–45. [CrossRef]
13. Rostamzadeh-Renani, M.; Baghoolizadeh, M.; Rostamzadeh-Renani, R.; Toghraie, D.; Ahmadi, B. The Effect of Canard’s Optimum Geometric Design on Wake Control Behind the Car Using Artificial Neural Network and Genetic Algorithm. *ISA Trans.* **2022**, *131*, 427–443. [CrossRef] [PubMed]
14. Baghoolizadeh, M.; Jasim, D.J.; Sajadi, S.M.; Renani, R.R.-; Renani, M.R.-; Hekmatifar, M. Using of Artificial Neural Networks and Different Evolutionary Algorithms to Predict the Viscosity and Thermal Conductivity of Silica-Alumina-MWCN/Water Nanofluid. *Heliyon* **2024**, *10*, e26279. [CrossRef]

15. Yang, L. Research on Design and Hydrodynamic Performance of "SEAGULL" Underwater Glider. Ph.D. Dissertation, Shanghai Jiao Tong University, Shanghai, China, 2017.
16. Chen, L.; Liu, R.; Guo, R.; Zhao, B.; Liu, L.; Yang, Y. Multi-Objective Optimization on Aerodynamic Shape of Projectile with Twisted Empennages. *Acta Armamentar.* **2016**, *37*, 1187–1193.
17. Zhu, H.; Liu, L.; Long, T.; Zhao, J. Global Optimization Method Using SLE and Adaptive RBF Based on Fuzzy Clustering. *Chin. J. Mech. Eng.* **2012**, *25*, 768–775. [CrossRef]
18. Pei, J.; Wang, W.; Yuan, S.; Zhang, J. Optimization on the Impeller of a Low-Specific-Speed Centrifugal Pump for Hydraulic Performance Improvement. *Chin. J. Mech. Eng.* **2016**, *29*, 992–1002. [CrossRef]
19. Zhang, F.; Wu, Q.; Zhao, X.; Liu, Y.; Wang, G. Multi-Objective Optimization of Inlet Duct of Water-Jet Propulsion Based on Response Surface Method. *Acta Armamentar.* **2020**, *41*, 2071–2080.
20. Jackson, I.R.H. Convergence Properties of Radial Basis Functions. *Constr. Approx.* **1988**, *4*, 243–264. [CrossRef]
21. Yang, Z.; Song, L. Integrated Design of Resistance and Manoeuvring Performances for Submersible Based on MOGA. *J. Ship Mech.* **2015**, *19*, 526–533.
22. Qian, L.; Chang, S.; Ni, Y. Multi-Objective Optimization of Aerodynamic Shape of Microspoiler for Spin-Stabilized Projectile. *Acta Armamentar.* **2021**, *42*, 2575–2585.